Complex Analysis of Askaryan Radiation: A Fully Analytic Treatment including the LPM effect and Cascade Form Factor

Jordan C. Hanson*

Center for Cosmological and AstroParticle Physics, Department of Physics, The Ohio State University, Columbus, OH 43210

Amy L. Connolly

Center for Cosmological and AstroParticle Physics, Department of Physics, The Ohio State University, Columbus, OH 43210

Abstract

The Askaryan effect describes coherent electromagnetic radiation from high-energy cascades in dense media with a collective charge. We present an analytic model of Askaryan radiation that accounts simultaneously for the three-dimensional form factor of the cascade, and the Landau-Pomeranchuk-Migdal effect. These calculations, and the associated open-source code, allow the user to avoid computationally intensive Monte Carlo cascade simulations. Searches for cosmogenic neutrinos in Askaryan-based detectors will benefit from computational speed, because scans of geometric parameter space are required to match neutrino signals. The Askaryan field is derived from cascade equations verified with Geant4 simulations, and compared with prior numerical and semi-analytic calculations. Finally, instructive cases of the model are transformed from the Fourier domain to the time-domain. Next-generation *in situ* detectors like ARA and ARIANNA can use analytic time-domain signal models to search for phase correlations with event candidates.

Keywords: Cosmogenic neutrinos, GZK Effect, Askaryan Effect

1. Introduction

The landmark observation of PeV neutrino interactions in Antarctic ice by the IceCube collaboration [1] has highlighted the urgency for progress in ultra-high energy cosmogenic neutrino

☆Open-source code associated with this work: https://github.com/918particle/AskaryanModule

*Corresponding author

Email address: hanson.369@osu.edu (Jordan C. Hanson)

(UHE-ν) searches, at energies $10^{16} - 10^{20}$ eV [2] [3] [4]. Cosmogenic neutrinos represent a long awaited prize in both astrophysics and particle physics, because of their potential to explain the origin of UHE cosmic rays (UHECR), as well as the chance to study electroweak interactions at record-breaking energies.

The GZK process is an example of a $p\gamma$ interaction yielding UHE-ν production from the cosmic ray flux on the cosmic microwave background [5] [6]. Most UHECR flux models lead to the conclusion that 100 km^3-volume detectors are required to measure the UHE-ν flux [7] [8] [9] [10]. UHE-ν also present the possibility revealing physics beyond the Standard Model, via measurements of UHE-ν deep-inelastic scattering cross-sections [11] [12]. Models matching simultaneously the PeV flux from IceCube, the diffuse GeV gamma-ray flux, and the UHECR flux, are now understood to constrain the UHE-ν flux [13] [9] [14].

A new generation of detectors for UHE-ν is based on the Askaryan effect, in which a UHE-ν interaction produces a cascade that radiates radio-frequency pulses from within a dielectric medium [15] [16] [17]. This growing class of experiments uses the special radio-frequency properties of Antarctic ice, in order to search for UHE-ν cascades efficiently [18] [19] [20]. The Radio Ice Cernekov Experiment (RICE) conducted the pioneering search [21]. The Antarctic Impulsive Transient Antenna (ANITA) is a balloon-borne detector [22] [23]. The Askaryan Radio Array (ARA), and the Antarctic Ross Ice Shelf Antenna Neutrino Array (ARIANNA) are two *in situ* detectors similar to RICE, but designed on a much larger scale [24] [25] [26] [27] [28]. The ExaVolt Antenna (EVA) is a proposed design to improve on the ANITA detection scheme, using the balloon itself as the antenna [29].

The Askaryan signal expected in each of these experiments must be understood in detail. Zas, Halzen, and Stanev (ZHS) created a Monte Carlo simulation which calculated the electric field by tracking the radiation from every cascade particle, using the Fraunhofer approximation [30]. This technique is computationally expensive, and cannot be scaled to UHE-ν energies. Semi-analytic models [31] [32] by J. Alvarez-Muniz, A. Romero-Wolf, R.A. Vazquez, and E. Zas (ARVZ) solve Maxwell's equations, treating the cascade charge excess as a source current. These models require only the *profile* of the negative charge excess. Semi-classical methods become fully analytic when the Greisen and Gaisser-Hillas calculations are used for the profile [33].

J. Ralston and R. Buniy (RB) [34] presented a fully analytic, complex analysis of Askaryan radiation, expanding around the global maximum of the cascade profile. This approach yields

theoretical insight into observable properties of the field, while matching the form of the ZHS particle-tracking Monte Carlo. The model includes an explanation of signal causality, and merges coherence zones in a continuous fashion. A proper handling of non-far-field coherence zones is vital for lowering energy thresholds in the *in situ* Askaryan detectors (ARA/ARIANNA), because the lowest-energy events, by definition, are only detectable above thermal thresholds when the neutrino vertex is in coherence zones other than the Fraunhofer zone. Lowering energy thresholds is important for capturing more UHE-ν signals, because the flux is expected to increase with decreasing energy.

The RB work, however, may be generalized to cascades with realistic shape, from the cascade form factor, from lateral charge diffusion, and cascade-elongation from the Landau-Pomeranchuk-Migdal (LPM) effect. In this work, a model is presented that begins with RB, and include these two major extensions. These two effects constrain the high-frequency Fourier modes and solid angle of the radiation. The model is checked against Geant4 simulations at high energies (> 1 PeV) using a pre-shower, sub-shower technique, performed on clusters at the Ohio Supercomputing Center. The results are shown to follow the Greisen electromagnetic shower geometry [35]. Finally, the Askaryan field is expressed in the time-domain under several scenarios, useful for digital signal processing and cross-correlation in experiments like ARA and ARIANNA.

2. Units, Definitions, and Conventions

All calculations in this work have been encapsulated into an open-source C++ class, available online [1]. The primary function of this code is to predict the electric fields that Askaryan-based detectors would detect. In all sections, this class will be called the *associated code*, or simply *the code*.

The coordinate systems are shown in Fig. 1a. Observer coordinates are un-primed, and charge excess coordinates are primed. The cascade current $\mathbf{J}(t)$ is described in Sec. 3.2, and will be called the instantaneous charge distribution (ICD) in subsequent sections. The vectors ρ and ρ' refer to the lateral distance from the cascade axis, and z and z' refer to the cascade axis. The origin for both systems is the location of the cascade maximum, with $z' = z = 0$ and $\rho = \rho' = 0$. The viewing angle is θ. Bold variables, and variables with a circumflex, $\hat{e}_i$, refer to vectors. The observer distance is

[1] https://github.com/918particle/AskaryanModule

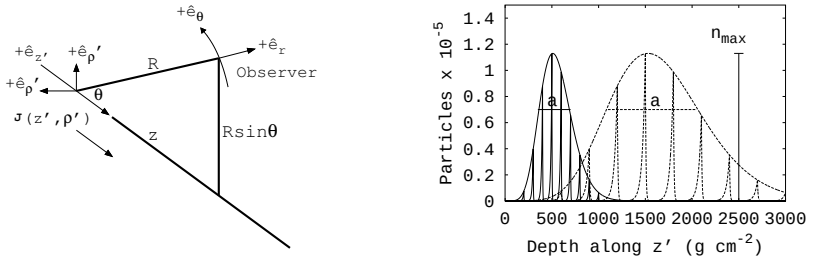

(a) (b)

Figure 1: (a) Coordinate systems. Un-primed coordinates refer to the observer, and primed coordinates refer to the reference frame of the vector current. (b) The curves represent the total charge content, with the instantaneous charge density (ICD) shown by the internal curves, versus depth after the first interaction in the medium. The solid curves were made for shower energy 10^{14} eV and the dashed curves for a shower profile having been stretched by either the LPM effect, or simply by going to a higher energy. The Greisen model was used for the form of the cascade profile. The $n_{\max}$ parameter will refer to the *negative* charge excess.

$R = |\mathbf{x} - \mathbf{x}'|$, ω refers to the angular frequency, and $k = (2\pi)/n\lambda$ and $\mathbf{q} = n(\omega R, \omega\rho)/(cR)$ refer to one- and three-dimensional wavevectors *in the dielectric*, with a refractive index n. Although the code takes $n = 1.78$ as a default value, it may be altered to apply to other uniform media. The Cherenkov angle is defined by the index of refraction: $\cos\theta_{\rm C} = 1/n$. The index of refraction at RF frequencies for bulk ice in Antarctica is 1.783 ± 0.003 [36].

The archetypal cascade profile is shown in Fig. 1b, in which the total number of cascade particles is shown, versus depth along the z' axis. The depth is Pz', where P is the bulk density of ice (0.917 g/cm^3). The parameter $n_{\max}$ will refer to the number of *negatively charged* particles (typically $\approx 20\%$ of the total - see Sec. 3.4.1 and the Appendix Sec. 7.3 for details). The parameter a is the Gaussian width of the cascade profile near cascade maximum. The cascade is initiated by an electroweak neutrino interaction, where the neutrino energy is E_ν, and the total energy of the cascade is $E_{\rm C}$.

The units of the electromagnetic field in the Fourier domain are V/m/Hz, often converted in the literature to V/m/MHz. To make the distance-dependence explicit, both sides of field equations are multiplied by R, making the units V/Hz. In Sec. 4, the field normalization constant is E_0, and it contains the energy-dependence. E_0 may be linearly scaled with energy, provided the parameters a and $n_{\max}$ are derived consistently from the Greisen model. Equations in Sec. 4 are proportional to ωE_0, so the units of E_0 are V/Hz^2.

In the original RB work, the following convention for the Fourier transform $\tilde{G}(\omega)$ of a function $g(t)$ was used:

$$\tilde{G}(\omega) = \int_{-\infty}^{\infty} e^{i\omega t} g(t) dt \tag{1}$$

$$g(t) = \frac{1}{2\pi} \int_{-\infty}^{\infty} e^{-i\omega t} \widetilde{G}(\omega) \tag{2}$$

The sign convention shown in the exponent is used in RB, though the opposite sign convention is more common in mathematical physics. The definitions in Eqs. (1, 2) have been kept for consistency with Sec. V of [34]. The sign convention may be toggled in the code, but the output does not depend on this choice, because the appropriate transformation in time is applied. All frequencies are shown in MHz in spectral plots, for comparison to the literature. The symbol $\sim$ above a function denotes a Fourier domain quantity. In Secs. 3.2 and 3.4, the three-dimensional Fourier transform is used to describe the form factor in three-dimensional frequency-space, with the normal sign convention:

$$\widetilde{F}(\mathbf{q}) = \int d^3x' f(\mathbf{x}') e^{-i\mathbf{q}\cdot\mathbf{x}'} \tag{3}$$

3. Combination of the RB model, the LPM Effect, and the Cascade Form Factor

In Sec. 3.1, the RB model [30] is presented for clarity, beginning with all assumptions made. Next, the model is enhanced by treating two new effects: *the LPM effect* (Sec. 3.3) and *the cascade form factor*, $\widetilde{F}$ (Sec. 3.4).

3.1. General Assumptions, and the Basic RB Model

The conventions are taken from Sec. 2 to build the RB model [34]. RB derive the Askaryan fields from Maxwell's equations in the Lorentz gauge for a dielectric medium, by expanding with a special scalar parameter η. The source current, $\mathbf{J}(t', \mathbf{x}')$, is described by an ICD $f(z' - vt, \rho')$, excess charge profile $n(z')$, and cascade speed $\mathbf{v}$:

$$\mathbf{J}(t', \mathbf{x}') = \mathbf{v} n(z') f(z' - vt, \rho') \tag{4}$$

$$\eta = \left(\frac{a}{\Delta z_{\text{coh}}} \right)^2 = \frac{k}{R} (a \sin\theta)^2 \tag{5}$$

The function $f(z'-vt,\rho')$ is the ICD and the Fourier transform of $f(z'-vt,\rho')$ is $\widetilde{F}(\omega)$. Equation 5 is the squared ratio of a, and $\Delta z_{\rm coh}$, the longitudinal range where the Askaryan radiation must be coherent. To understand $\Delta z_{\rm coh}$, consider Feyman's formula [30]. Radiation from an accelerating point charge is proportional to the angular acceleration $\ddot{\theta}$ relative to the observer. The coherence regime is defined by $|z'| \lesssim \Delta z_{\rm coh}$, where $\ddot{\theta}$ and $R(z')$ are constant in time to first order, and $\ddot{\theta}$ is maximized. RB show that if $R(z') < \lambda$ in this limit, $\Delta z_{\rm coh} < \sqrt{R/(k\sin^2\theta)}$.

The dominant Askaryan radiation arises from the portion of the shower profile satisfying $|z'| \lesssim \Delta z_{\rm coh}$. In either the Fresnel or Fraunhofer regimes, $\eta < 1$, but the RB model is not restricted to $\eta < 1$. The calculations should be valid for any η value, rather than the pure far-field approximation ($\eta \to 0$, and $kR \gg 1$, $R \gg a$). If $a \ll \Delta z_{\rm coh}$, then the fields have spherical symmetry and the limit $kR \gg 1$ corresponds to the Fraunhofer approximation. Conversely, if $a \gg \Delta z_{\rm coh}$, then $\eta \to \infty$, the fields have cylindrical symmetry, and $kR \gg 1$ corresponds to the Fresnel limit.

The longitudinal cascade width a, and therefore η, is derived in the code from either the Greisen or Gaisser-Hillas cascade profile functions (Secs. 3.4-3.4.1), and can be modified by the LPM effect. The Greisen function represents electromagnetic cascades, and the Gaisser-Hillas hadronic cascades. The associated code requires the type of cascade profile as an input, and whether the LPM effect must be applied.

3.2. The RB Field Equations

RB insert the vector current $\mathbf{J}(t',\mathbf{x}')$ into Maxwell's equations, and solve for the vector potential:

$$c\mathbf{A}(\mathbf{x}') = \int d^3x' \frac{e^{ik|\mathbf{x}-\mathbf{x}'|}}{|\mathbf{x}-\mathbf{x}'|} \int dt' e^{i\omega t'} \mathbf{J}(t',\mathbf{x}') \tag{6}$$

RB then define $R(z') = \sqrt{(z-z')^2+\rho^2}$), and expand around $\rho' = 0$:

$$|\mathbf{x}-\mathbf{x}'| \approx R(z') - \frac{\rho\cdot\rho'}{R(z')} + \frac{\rho'^2}{2R(z')} \tag{7}$$

In Eq. 7, the third term on the right-hand side is dropped, because $\rho' \ll R(z')$. The vector potential in Eq. 6 is then factored into the form factor $\widetilde{F}(\omega)$ and a vector function. $\widetilde{F}(\omega)$ is the three-dimensional Fourier transform of the ICD, and the vector is governed by $n(z')$. *Thus,* $\widetilde{F}(\omega)$ *describes the charge distribution, and the vector portion describes the charge evolution.* Equations 8-9 summarize the result. In Eqs. 8-9, $\widetilde{\mathbf{A}}^{FF}$ is the vector potential, named the *Fresnel-Fraunhofer* (FF) potential in RB.

$$\widetilde{\mathbf{A}}(\omega,\theta) = \widetilde{\mathbf{A}}^{FF}(\omega,\theta)\int d^3x' e^{-i\mathbf{q}\cdot\mathbf{x}'} f(\mathbf{x}') \tag{8}$$

$$\widetilde{\mathbf{A}}(\omega,\theta) = \widetilde{F}(\omega,\theta)\widetilde{\mathbf{A}}^{FF}(\omega,\theta) \tag{9}$$

Equations 10-13 express the general RB result for the electric field $\mathbf{E} = -\partial\mathbf{A}/\partial t$, in terms of the frequency ν, viewing angle θ, and η:

$$\frac{R\widetilde{\mathbf{E}}(\nu,\theta,\eta)}{\left[\frac{\mathrm{V}}{\mathrm{MHz}}\right]} = 2.52\times10^{-7}\frac{a}{[\mathrm{m}]}\frac{n_{\max}}{[1000]}\frac{\nu}{[\mathrm{GHz}]}\widetilde{F}(\mathbf{q})\psi\boldsymbol{\mathcal{E}} \tag{10}$$

$$\psi = -ie^{ikR}\sin\theta \tag{11}$$

$$\boldsymbol{\mathcal{E}} = \mathcal{W}(\eta,\theta)\left(\frac{\cos\theta_{\mathrm{C}}-\cos\theta}{\sin\theta}\right)\hat{e}_{\mathrm{r}} + \mathcal{W}(\eta,\theta)\left(1-i\eta\frac{\cos\theta_{\mathrm{C}}}{\sin^2\theta}\frac{\cos\theta-\cos\theta_{\mathrm{C}}}{1-i\eta}\right)\hat{e}_{\theta} \tag{12}$$

$$\mathcal{W}(\eta,\theta) = \left(1-i\eta\left(1-3i\eta\frac{\cos\theta}{\sin^2\theta}\frac{\cos\theta-\cos\theta_{\mathrm{C}}}{1-i\eta}\right)\right)^{-1/2}\exp\left(-\frac{1}{2}(ka)^2\frac{\cos\theta-\cos\theta_{\mathrm{C}}}{1-i\eta}\right) \tag{13}$$

Equation 10 is the total field, with a overall phase factor defined in Eq. 11. Equation 12 contains the vector structure, and Eq. 13 governs the phase and angular structure.

3.3. The Landau-Pomeranchuk-Migdal (LPM) Effect

The Landau-Pomeranchuk-Migdal effect, or LPM effect, suppress the pair-creation and bremsstrahlung cross-sections at cascade energies above a material-dependent constant known as the LPM energy or E_{LPM} [37]:

$$E_{\mathrm{LPM}} = \frac{(mc^2)^2\alpha X_0}{4\pi c\hbar} = 7.7\ \mathrm{TeV/cm}\cdot X_0 \tag{14}$$

In Eq. 14, m is the electron mass, α is the fine-structure constant, and X_0 is the radiation distance ($E_{\mathrm{LPM}} = 0.303$ PeV for ice). If the particle energy is greater than E_{LPM}, the quantum mechanical *formation length* of typical bremsstrahlung and pair-production interactions is longer than atomic separations, leading to quantum interference that suppresses cross-sections. The result is a *longitudinal shower elongation*, from the non-interacting, higher-energy particles. The LPM effect is reviewed by S.R. Klein in Ref. [37], and Ref. [38] explains how LPM physics may be added to the ZHS MC approach.

The LPM changes how the RB model must be applied. Under normal circumstances, the quantity $n_{\max}a$ approximates the area under the cascade profile, or the total number of cascade particles. RB note that, for particles with energy greater than some critical energy $E_{\rm crit}$, $a \propto \sqrt{\ln(E_C/E_{\rm crit})}$ and $n_{\max} \propto (E_{\rm C}/E_{\rm crit})/\sqrt{\ln(E_{\rm C}/E_{\rm crit} - 0.33)}$, so $n_{\max}a \propto E_{\rm C}$, for the Greisen cascade parameterization. It is shown in Ref. [39] that in the LPM-regime, $a \propto \sqrt{E_{\rm C}/E_{\rm crit}}$. While it may appear that changing the energy scaling of a violates energy conservation through the field normalization $n_{\max}a$, this is not the case.

First, the amount of *radiated* energy does not have to correspond to the cascade energy, if the shape of the cascade is modified. The Frank-Tamm formula for a uniform charge moving at a finite track [34] shows that the radiated goes like $d^2P/d\Omega d\omega \propto L^2$, for track-length L. The LPM effect elongates L, so a relative increase in the radiated energy should be expected, provided the track is within $\Delta z_{\rm coh}$. It is shown in Sec. 4 that enhancements due to cascade elongation are limited by a coherence frequency, the cascade form factor, or both. Also, there is additional limitation in radiated power through the reduction of the angular width of the Cherenkov cone under the influence of the LPM effect (see Appendix Sec. 7.2).

Second, there is no reduction in $n_{\max}$ that corresponds to the relative increase in a. Figures 12 and 13 of Ref. [40] demonstrate that the electromagnetic cascades elongate while accounting for the LPM effect, but that the dependence of $n_{\max}$ on the shower energy is not reduced. Figure 12 of Ref. [40] shows that the cascade maximum location grows and fluctuates more strongly at energies above $E_{\rm LPM}$. However, Fig. 13 of Ref. [40] shows that the energy dependence of $n_{\max}$ stays approximately the same, and $n_{\max}$ fluctuates mildly for $E_{\rm C}$ in the GZK primary energy range. Physically, all cascade particle energies must eventually decrease to below $E_{\rm LPM}$ in a cascade. By definition, this must take place before the cascade maximum, so to first order $n_{\max}$ is actually governed by standard cascade physics, even when $E_{\rm C} > E_{\rm LPM}$ initially.

S.R. Klein notes in Ref. [37] that the LPM effect may influence the form factor, $\widetilde{F}(\omega)$. $\widetilde{F}(\omega)$ is controlled by the lateral ICD, from multiple scattering (MSC) effects that lead to a mean scattering angle $\langle\theta_{\rm MSC}\rangle$ for cascade particles incident on atoms in the medium [37] [35]. $\langle\theta_{\rm MSC}\rangle$ takes the following form for a particle of energy E:

$$\langle\theta_{\rm MSC}\rangle = \frac{E_{\rm s}}{E}\sqrt{\frac{d}{X_0}} \tag{15}$$

X_0 is the radiation length in units of distance, and d is the distance over which the scattering

occurs, and $E_{\rm s}$ is the Molière scattering energy, where $E_{\rm s} = mc^2\sqrt{4\pi/\alpha} \approx 21.2$ MeV. The LPM effect increases d relative to X_0, increasing $\langle\theta_{MSC}\rangle$. Although $\langle\theta_{\rm MSC}\rangle$ is enhanced by the LPM effect, it is also inversely proportional to energy. This implies that the inevitable pile-up of particles with energy $E_{\rm crit} \approx E_{\rm s}$ actually governs the ICD width, at a point in the cascade when the LPM effect is no longer important.

Finally, a remark about "shower fluctuations" is prudent. First, while the LPM effect may cause the depth of the cascade maximum to fluctuate (see Fig. 12 of Ref. [40]), the *location* of cascade maximum is irrelevant for Askaryan radiation, just as any radiation field is independent of the origin of the coordinate system. The origin in the associated code is the location of cascade maximum, *wherever it occurs*. Much harder to model is the effect of the multi-peaked cascade profile typical of LPM-induced fluctuations. This can lead to a reduction in the Cherenkov cone-width, and further modified by the elongated tail of the cascade profile [41]. However, it is shown in Ref. [42] that the sub-peaks only alter the waveform in limited circumstances, such as being off-cone by $\approx 10^\circ$, and in the Fraunhofer regime. The waveforms in Ref. [42] all contain the basic bi-polar structure produced by the associated code, despite the multi-peaked cascade profile.

In summary, the main effect LPM physics has on Askaryan radiation is the filtering via the elongation of the cascade profile. The associated code quantifies this by elongating the shower width a, using calculations by Klein and Gerhardt shown in Fig. 2 [39]. In scenarios where LPM is unimportant (initial hadronic-dominated processes [41], cascades with $E_{\rm C} < E_{\rm LPM}$), the associated code draws the width and height of the negative charge excess profile from the usual Greisen and Gaisser-Hillas formulations [35] [43].

3.4. The Cascade Form Factor, $\widetilde{F}$

The factorization of the longitudinal charge excess *evolution*, $\widetilde{\mathbf{A}}^{FF}(\omega,\theta)$, and the instantaneous properties of the lateral charge *distribution*, $\widetilde{F}(\omega)$, leads to the interpretation of $\widetilde{F}(\omega)$ as a filter. Filters are fully described by *pole-zero* diagrams, which display the Laplace transform of the filter transfer function. Impulsive E-fields with no DC-component automatically approach 0 as $|\omega| \to 0$, meaning $\widetilde{F}$ should not require any zeros. Thus, $\widetilde{F}(\omega)$ should be completely defined by poles in the complex ω-plane.

D. Garcia-Fernandez *et. al.* (Ref. [44]) show that the integrals over individual tracks in the ZHS algorithm can be generalized to all coherence regimes, when integrated numerically. The authors

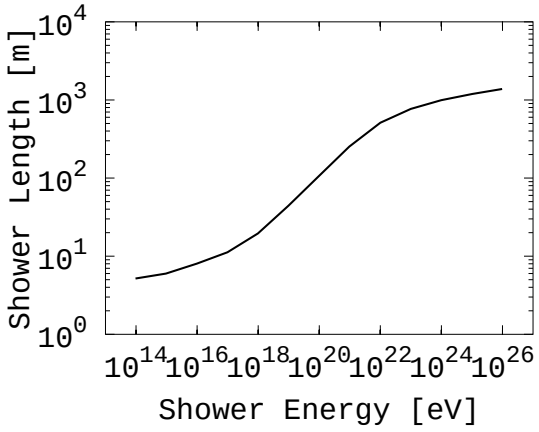

Figure 2: The length of the neutrino-induced cascade, including the LPM effect, from ref. [39].

of Ref. [44] then insert the form factor chosen in Ref. [45] into the RB framework to demonstrate agreement (Fig. 7 of Ref. [44]). This agreement occurs at frequencies below 120 MHz, below the bandwidths of ARA/ARIANNA. The lateral ρ'-dependence of the chosen form factor is gaussian ($f \propto \exp(-\rho'^2)$), yielding gaussian behavior in the Fourier domain ($|\widetilde{F}| \propto \exp(-\omega^2)$). Geant4 simulations and the Greisen model show that $f(\mathbf{x}')$ is not gaussian (Sec. 3.4.1 and Appendix Sec. 7.3). Additionally, the ultra-violet divergence in Ref. [44] is attributed to the assumption that the dielectric constant $\epsilon(\omega)$ is not absorptive, however, the effect of $\widetilde{F}(\omega)$ is apparent in that model near 1 GHz. This is because the filtering effect of $\widetilde{F}(\omega, \theta)$ occurs when the Askaryan radiation of all finite tracks in a cascade are summed.

The ZHS form factor, $\widetilde{F}_{\mathrm{ZHS}}(\omega)$, is constructed of poles which imply that the lateral ICD $f \propto \exp(-\rho')$. The key result for $\widetilde{F}(\omega)$ is given in Eq. 16, in terms of the viewing angle θ, the angular frequency ω, and $(\sqrt{2\pi}\rho_0)^{-1}$, the distance from the cascade axis ($\rho' = 0$) at which the negative charge excess has decreased by $1/e$.

$$\widetilde{F}(\omega, \theta) = \frac{1}{\left(1 + \left(\frac{(\omega/c)\sin\theta}{\sqrt{2\pi}\rho_0}\right)^2\right)^{3/2}} \tag{16}$$

Intuitively, the squared ratio in the denominator of Eq. 16 compares the lateral projection of the wavevector with the physical extent of the charge excess. If the charge excess is laterally large, compared to the wavelength, then Eq. 16 begins to act as a low-pass filter. *By substituting Eq.*

16 into Eq. 10, the RB model is completed, properly accounting for LPM elongation and the ICD. The form factor $\widetilde{F}(\omega, \theta)$ is derived from fits to Geant4 cascades, for $E_{\rm C} = 1 - 100$ PeV. Once the quality of these fits is established, one may proceed with the theoretical cascade models, with no need of further numerical simulation.

3.4.1. The Greisen Model

K. Greisen provided a comprehensive review of the longitudinal charge evolution, and lateral distribution, within electromagnetic cascades [35], by combining earlier work by Molière, Nishimura and Kamata, Landau, and others. The integrated charge at depth z_0 in the medium is

$$n_{\rm tot}(z_0) = \frac{0.31}{\sqrt{\ln(E_{\rm C}/E_{\rm crit})}} \exp\left\{ z_0 \left(1 - \frac{3}{2} \ln(s) \right) \right\} \tag{17}$$

In Eq. 18, z_0 is in units of radiation length (36.08 g cm^{-2}), and the cascade energy $E_{\rm C}$ in units of GeV ($E_{\rm crit} = 73$ MeV) [30, 33]. The *shower age* is $s = 3z_0/(z_0 + 2\ln(E_{\rm C}/E_{\rm crit}))$. Equation 17 is most accurate near shower maximum: $z_{\rm max} = \ln(E_{\rm C}/E_{\rm crit})$. K. Greisen showed that $\langle \ln n_{\rm tot} \rangle \approx 0.7(s - 1 - 3\ln s)$. When $s = 1$ at $z_{\rm max}$, $\langle \ln n_{\rm tot} \rangle = 0$, implying negligible fluctuation in $n_{\rm max}$. It may be shown that $a \propto \sqrt{z_{\rm max}}$ [34]. For $n_{\rm max} = n_{\rm tot}(z_{\rm max})$, $n_{\rm max} a \propto E_{\rm C}/E_{\rm crit}$. The factor $n_{\rm max} a$ approximates the area under the peak of Eq. 17, and is proportional to $E_{\rm C}$ for $E_{\rm C} \lesssim E_{\rm LPM}$. The scaling becomes steeper under the influence of the LPM effect (Fig. 2). The cascade lives longer, so a higher fraction of $E_{\rm C}$ is radiated rather than deposited in the ice.

The lateral ICD arises from multi-scattering effects (MSC processes in Geant4), with average scattering angle $\langle \theta_{\rm MSC} \rangle$ (Eq. 15), and a Molière radius defined by $\rho_1 = E_{\rm MSC}/E_{\rm c}$, in radiation lengths. Large errors arise for angles $\theta \gg \langle \theta_{\rm MSC} \rangle$, or ($\rho' > \rho_1$), but few particles have $\rho' > \rho_1$. The $\langle \theta_{\rm MSC} \rangle$ is expressed in Eq. 18, for particles of energy ϵ in electromagnetic cascades [37]:

$$\langle \theta_{\rm MSC} \rangle = \frac{E_{\rm MSC}}{\epsilon} \sqrt{z_0} = \frac{m_e c^2 \sqrt{4\pi z_0/\alpha}}{\epsilon} \approx \frac{21.2\,[\text{MeV}]}{\epsilon} \sqrt{z_0} \tag{18}$$

Equation 18 implies the lateral ICD should be widest near $n_{\rm max}$, where the average particle energy is minimized. The lag in z' of most particles with respect to the cascade front is $\mathcal{O}(1 - 10)$ cm at $n_{\rm max}$. This lag is described in Eq. 13 of [37], assuming that particles at ρ' have equal s. Nishimura and Kamata refine the approximation, provide the lateral charged particle density, D,

and the result is known as the NKG-function, shown in Eq. 19.

$$D = \frac{n_{\text{tot}}}{2\pi\rho_1^2}\frac{\Gamma(4.5-s)}{\Gamma(s)\Gamma(4.5-2s)}\left(\frac{\rho'}{\rho_1}\right)^{s-2}\left(1+\frac{\rho'}{\rho_1}\right)^{s-4.5} \tag{19}$$

Numerical results in the Appendix Sec. 7.3 show that this work agrees with Eqs. 17-19, and the ICD is assigned a three-dimensional function $f(\mathbf{x}')$. In Sec. 3.4.2, $\widetilde{F}(\omega)$ is derived analytically from $f(\mathbf{x}')$. For details on the ICD, $f(\mathbf{x}')$, see the Appendix Sec. 7.3. Other efforts to model the ICD and the resulting Askaryan radiation can be found in Refs. [46, 47, 48].

3.4.2. Analytic Formula for $\widetilde{F}(\omega,\theta)$

The definition of $\widetilde{F}(\omega,\theta)$ is

$$\widetilde{F}(\mathbf{q}) = \int d^3x' e^{-i\mathbf{q}\cdot\mathbf{x}'} f(\mathbf{x}') \tag{20}$$

The ICD $f(\mathbf{x}')$ is given by a general parameterization of the Greisen model:

$$f(\mathbf{x}') = \rho_0^2\delta(z')\exp(-\sqrt{2\pi}\rho_0\rho') \tag{21}$$

The choice of Eq. 21 is motivated in the Appendix Sec. 7.3. Recall that the ICD is meant to describe the number density of the negative charge excess, not the total charged particle number density. Geant4 MC calculations and the Greisen model predict the exponential form, and the ZHS parameterization suggests it in the Fourier domain. C.-Y. Hu *et al* chose a double-Gaussian form [45], which is not accurate near $\rho' = 0$, but highlights the relationship between theoretical parameters and numerical fields. Note that the units of the $1/e$ width $\sqrt{2\pi}\rho_0$ and $\delta(z')$ are inverse length, giving $f(\mathbf{x}')$ units of number density.

Fitted results for the parameter $\sqrt{2\pi}\rho_0$ for times between 20-30 ns ($s \approx 1$) indicate that $\sqrt{2\pi}\rho_0 \sim$ is constant with respect to cascade depth. The solution to Eq. 20 is as follows: the trivial z' integration is performed, setting $z' = 0$ without loss of generality. Next, two convenient variables are defined, and shown in Eqs. 22 and 23.

$$\gamma = \frac{\omega}{c}\sin\theta \tag{22}$$

$$\sigma = \frac{\gamma}{\sqrt{2\pi}\rho_0} \tag{23}$$

The variable γ is the lateral projection of the wavevector, and σ is the product of γ and the lateral charge extent. The variable σ compares the laterally-projected wavelength to the lateral extent of cascade excess charge. In Sec. 4, $\sigma = \omega/\omega_{\rm CF}$, so that $\omega_{\rm CF}$ is the limiting frequency. Substituting Eqs. 21, 22 and 23 into Eq. 20, $\widetilde{F}(\omega,\theta)$ becomes

$$\widetilde{F}(\omega,\theta) = \rho_0^2 \int_0^\infty d\rho' \rho' \exp\left\{-\frac{\gamma}{\sigma}\rho'\right\} \int_{-\pi}^{\pi} d\phi' \exp\left\{-i\rho'\gamma\cos(\phi')\right\} \tag{24}$$

From the cylindrical symmetry of $f(\mathbf{x}')$, the ϕ' coordinate may be rotated. With $\phi' \to \phi' - \pi/2$, the ϕ'-integral becomes a 0th-order Bessel function. A similar result in Ref. [46] contains the Bessel function in Eq. 24. In Ref. [46], however, the lateral ICD is not evaluated analytically, but through numeric integrals. After making the substitution $u' = \gamma\rho'$, the remaining ρ'-integral may be found in standard tables.

$$\widetilde{F}(\omega,\theta) = \sigma^{-2} \int_0^\infty du' u' \exp\left\{-\frac{u'}{\sigma}\right\} J_0(u') \tag{25}$$

$$\widetilde{F}(\omega,\theta) = \frac{1}{(1+\sigma^2)^{3/2}} \tag{26}$$

The result for $\widetilde{F}(\omega,\theta)$ is shown in Eq. 26. The Askaryan spectrum is attenuated like ω^{-3} for $\sigma \gg 1$, for wavelengths much smaller than the lateral ICD. For $\sigma \lesssim 1$, $\widetilde{F}(\omega,\theta) \approx (1 + (3/2)\sigma^2)^{-1}$. Given the the location of complex poles for $\sigma \ll 1$, one might suspect problems with causality. It is important to note, upon transforming the model to the time domain, including the LPM effect and the effect of $\widetilde{F}(\omega,\theta)$, that the fields do not violate the causality criterion stated by RB [34].

Equation 16 in Ref. [31] contains the Askaryan vector potential versus retarded time ($t_{\rm r}$), matched to MC at $\theta = \theta_C$, with six numerical parameters, not counting the overall normalization. This equation is restated as Eq. 27, and the $x_{\rm i}$ have unique values for $t_{\rm r} > 0$ and $t_{\rm r} < 0$.

$$\frac{R\mathbf{A}(t_{\rm r},\theta_{\rm C})}{[\mathrm{V}\cdot\mathrm{s}]} = -E_0' \sin(\theta_{\rm C})\hat{e_\theta} \left(\exp(-2|t_{\rm r}|/x_0) + (1 + x_1|t_{\rm r}|)^{-x_2}\right) \tag{27}$$

Equation 26 fully describes the cascade shape, is analytic, and, when combined with $\widetilde{\mathbf{A}}^{FF}$, produces fields that obey causality (see Sec. 3.5). Additionally, $\widetilde{F}$ only needs one MC constant: $\sqrt{2\pi}\rho_0$. Although the second term in Eq. 27 accounts for the asymmetric MC vector potential in an ad-hoc fashion, this asymmetry flows directly from Eq. 26 (Sec. 4), and special cases of the $x_{\rm i}$

are derived. Rather than requiring six raw MC numbers, the associated code relies on Eq. 26, and one MC parameter ($\sqrt{2\pi}\rho_0$).

3.4.3. Generalization of Eq. 26

In the Appendix Sec. 7.3, the lateral distribution of excess charge near cascade maximum is shown to follow Eq. 21 for $\rho' < \rho_1$, where ρ_1 is the Molière radius. To include the effect of charges beyond a single Molière radius, the following form for $f(\mathbf{x}')$ may be taken:

$$f(\mathbf{x}') = \delta(z') \sum_{\mathrm{i}}^{N} a_{\mathrm{i}} \exp(-\sqrt{2\pi}\rho_{\mathrm{i}}\rho') \tag{28}$$

The normalization requirement for the ICD provides the following constraint on the $2N$ free parameters:

$$\sum_{\mathrm{i}}^{N} \left(\frac{a_{\mathrm{i}}}{\rho_{\mathrm{i}}^2} \right) = 2\pi \tag{29}$$

Note that the units of the a_{i} parameters are the same as the normalization ρ_0^2 in the single-exponential case. Let α_{i} and σ_{i} take the following definitions:

$$a_{\mathrm{i}} = \alpha_{\mathrm{i}} \rho_{\mathrm{i}}^2 \tag{30}$$

$$\sigma_{\mathrm{i}} = \frac{\gamma}{\sqrt{2\pi}\rho_{\mathrm{i}}} \tag{31}$$

With this definition, Eq. 26 may be generalized to arbitrary Molière radii, taking the following form:

$$\widetilde{F}(\omega, \theta) = \sum_{\mathrm{i}}^{\mathrm{N}} \frac{\alpha_{\mathrm{i}}}{(1 + \sigma_{\mathrm{i}}^2)^{3/2}} \tag{32}$$

It is shown in Sec. 4.2 that in the far-field limit, at $\theta = \theta_{\mathrm{C}}$, the effect of extending the form factor $\widetilde{F}$ to arbitrary Molière radii is equivalent to adding a set of additional poles to the Askaryan field in the complex ω-plane. In the time domain, the Askaryan field picks up a series of exponential terms corresponding to the added poles.

3.5. Results of the Model: RB+LPM+$\widetilde{F}(\omega,\theta)$

The associated code output, including all effects, for $\hat{e}_\theta \cdot \mathbf{E}(t)$ is shown in Fig. 3, with $E_{\rm C} = 1000$ PeV. Figure 3 contains contour graphs, in units of mV/m, versus the retarded time in nanoseconds, and θ in degrees. The quadratic grey dashed line on the contours is a causal requirement from RB, showing how the arrival time (e.g. group delay) of the signal depends on θ. *Phase delays* t_ϕ about the quadratic are allowed: $t_\phi = -\phi(\omega)/\omega$. Phase delays are most prominent when $\widetilde{F} \neq 1$, $\theta \neq \theta_{\rm C}$, and when the LPM effect is strong. See Appendix Sec. 7.2 for further detail.

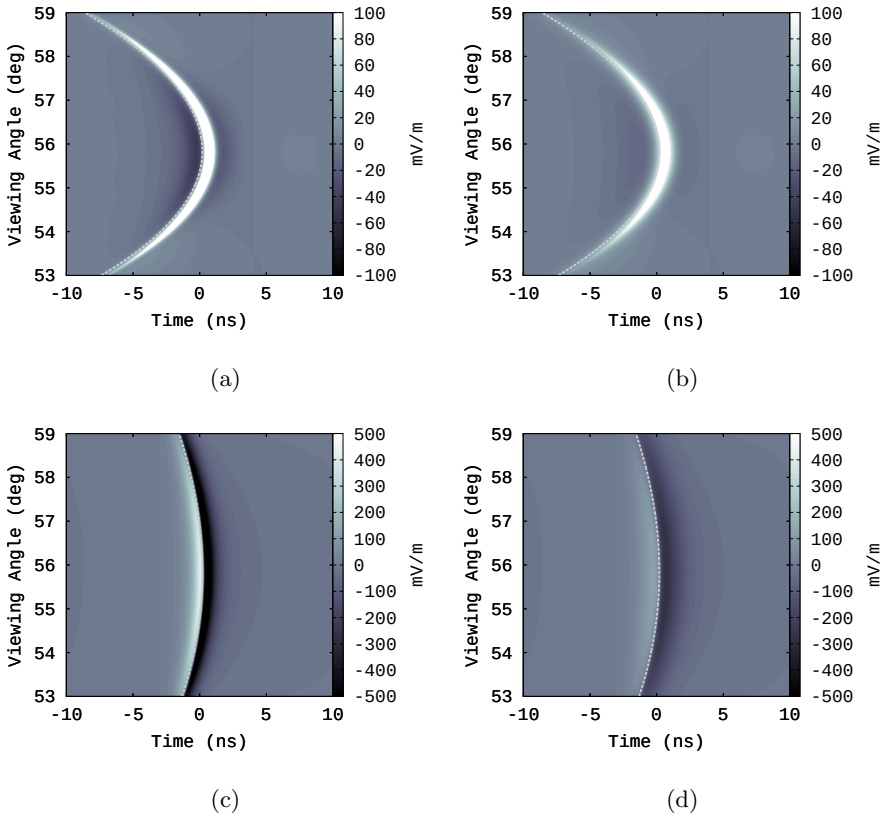

Figure 3: Contours of $\hat{e}_\theta \cdot \mathbf{E}(t)$, for a cascade energy of 1000 PeV. (a) R=1000 m, lateral ICD width of 5 cm. (b) R=1000 m, lateral ICD width of 10 cm. (c) R=200 m, lateral ICD width of 5 cm. (d) R=200 m, lateral ICD width of 10 cm. The LPM effect has been taken into account. See text for details.

The fields are shown for $R = 200$ m and 1000 m, $(\sqrt{2\pi}\rho_0)^{-1} = 5$ cm and 10 cm in Fig. 3. The causality requirement from RB leads to off-cone regions have a higher effective velocity. A larger

R value leads to wider separation in arrival times, as these off-cone modes have longer to outpace the other modes (earlier times correspond to more negative retarded times).

An enticing implication of the effective velocity variation is that the degeneracy between a low-energy event interacting close to the observer, and a high-energy event interacting correspondingly farther from the observer would be broken. Recall that $\widetilde{\mathbf{E}} \propto R^{-1}$ in the far-field. An event with $R = 100$ m and $E_{\rm C} = 10$ PeV would have the same amplitude as an event with $R = 1000$ m and $E_{\rm C} = 100$ PeV, neglecting secondary effects like ice absorption. The temporal signature shown by the quadratics in Fig. 3 would be different in the two cases.

From Eq. 12, the field $\widetilde{\mathbf{E}}$ has both $\hat{e}_{\rm r}$ and $\hat{e}_\theta$ components. For the extreme Fraunhofer limit, as $\eta \to 0$, the ratio of the amplitudes of these components is independent of frequency:

$$\frac{\hat{e}_{\rm r} \cdot \widetilde{\mathbf{E}}}{\hat{e}_\theta \cdot \widetilde{\mathbf{E}}} = -\left(\frac{\cos\theta - \cos\theta_{\rm C}}{\sin\theta}\right) \tag{33}$$

Equation 33 shows that the $\hat{e}_{\rm r}$-component of $\mathbf{E}(t)$ is positive above the Cherenkov angle, and negative below it. Since the $\hat{e}_{\rm r} \cdot \mathbf{E}(t) = 0$ at θ_C, the maximum in the $\hat{e}_{\rm r}$-component is always at some angle $\theta \neq \theta_C$. The contour graphs of Fig. 4 represent the $\hat{e}_{\rm r}$-component of the same fields as Fig. 3. Because $\hat{e}_{\rm r} \cdot \widetilde{\mathbf{E}} < \hat{e}_\theta \cdot \widetilde{\mathbf{E}}$, the Askaryan field is usually given with a pure $\hat{e}_\theta$-polarization. Though the $\hat{e}_{\rm r}$-component is small compared to the $\hat{e}_\theta$-component, the code does not neglect it. The polarization ratio (Eq. 33) is both complex, and frequency-dependent if $\eta \neq 0$.

4. Time-Domain Properties at the Cherenkov Angle

The analytic RB+LPM+$\widetilde{F}(\omega,\theta)$ model is derived in the time-domain for limiting cases, and parameters from the semi-analytic treatment in Ref. [31] are derived analytically. The authors of [46] provide a similar formula for $\widetilde{F}(\omega)$, but resort to MC techniques to fit that formula to MC results. The authors of [45] made the wrong choice for the form of the ICD (see Sec. 3.4.2).

Two cases are considered: $\widetilde{F} = 1$, followed by $\widetilde{F}(\omega,\theta) \neq 1$. The limiting frequency of the former, $\omega_{\rm C}$, is governed by coherence. The latter has two limiting frequencies, $\omega_{\rm C}$ and $\omega_{\rm CF}$, which leads to an asymmetry in the vector potential, and therefore, asymmetry in $\widetilde{\mathbf{E}}$. The SI units of terms like $R\widetilde{\mathbf{E}}$ in the Fourier domain are [V/Hz], while they are just [V] for $R\mathbf{E}$ in the time-domain. The overall scale of the field is not relevant in this section, so the unit of frequency is left as [Hz], rather than [MHz]. In each derivation, the viewing angle is $\theta = \theta_{\rm C}$.

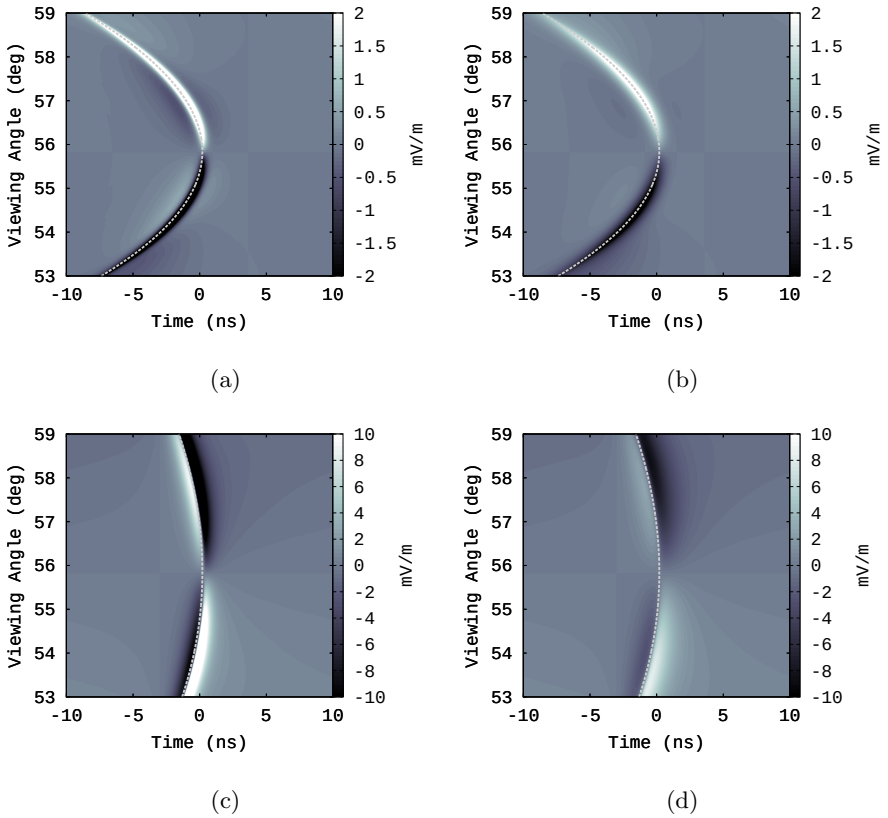

Figure 4: Contours of $\hat{e}_{\rm r} \cdot \mathbf{E}(t)$, for a cascade energy of 1000 PeV. (a) R=1000 m, lateral ICD width of 5 cm. (b) R=1000 m, lateral ICD width of 10 cm. (c) R=200 m, lateral ICD width of 5 cm. (c) R=200 m, lateral ICD width of 10 cm. In all cases, the gray dashed line represents the causality requirement. See text for details.

4.1. The limit $\eta < 1$, $\widetilde{F}(\omega, \theta_{\rm C}) = 1$

Recall from Eq. 10 of Sec. 3.2 that the vector-form of the on-cone field from the RB formalism takes the form:

$$\frac{R\widetilde{\mathbf{E}}(\omega, \theta_{\rm C})}{[\rm V/Hz]} = -\frac{i\omega E_0 \sin\theta_{\rm C} e^{i\omega R/c}}{(1 - i\eta)^{1/2}} \hat{e_\theta} \tag{34}$$

Let $\hat{E_0} = E_0 \sin\theta_{\rm C} \hat{e}_\theta$, and define ω_C from η: $\eta = \omega/\omega_{\rm C}$. Equation 34 may be approximated to first order in the limit $\eta < 1$, or $\omega < \omega_{\rm C}$, equivalent to requiring $\lambda R \gtrsim 5a^2$. Using the definition of

η, $\nu_{\rm C} = \omega_{\rm C}/(2\pi)$ is

$$\nu_{\rm C} = \frac{cR}{2\pi a^2 \sin^2\theta_{\rm C}} \tag{35}$$

Applying the given limit to Eq. 34, and taking the inverse Fourier transform, yields

$$R\mathbf{E}(t_{\rm r},\theta_{\rm C}) \approx \frac{i\omega_{\rm C}\hat{E}_0}{\pi}\frac{d}{dt_{\rm r}}\int_{-\infty}^{\infty} d\omega \frac{e^{-it_{\rm r}\omega}}{\omega + 2i\omega_{\rm C}} \tag{36}$$

The sign convention in the exponential in Eq. 36 is chosen to remain consistent with the RB formalism. The integral may be performed using the Cauchy integral formula, provided that the numerator is analytic ($\exp(-i\omega t_{\rm r})$ obeys the Cauchy-Riemann equations).

Contour integration of Eq. 36 requires a contour C that satisfies Jordan's lemma and includes all $\omega \in \mathrm{Re}\{\omega\}$. For the $t_{\rm r} > 0$ case, the integral converges along the contour defined by the infinite lower semi-circle because the magnitude of the numerator decreases like $\exp(\mathrm{Im}\{\omega\})$. Note that this is a negatively-oriented contour. For the case $t_{\rm r} < 0$, use the fact that $\mathcal{F}_\omega(x(-t)) = \widetilde{X}(-\omega)$, so $x(-t) = \mathcal{F}_\omega^{-1}(\widetilde{X}(-\omega))$, where $\mathcal{F}_\omega(x) = \widetilde{X}(\omega)$ is the Fourier transform of a function $x(t)$. The final solution is piecewise:

$$\frac{R\mathbf{E}(t_{\rm r},\theta_{\rm C})}{[\mathrm{V}]} \approx 4\hat{E}_0\omega_C^2 \begin{cases} \exp(2\omega_{\rm C}t_{\rm r}) & t_{\rm r} \le 0 \\ -\exp(-2\omega_{\rm C}t_{\rm r}) & t_{\rm r} > 0 \end{cases} \tag{37}$$

MC calculations show the transition at $t_{\rm r} = 0$ to be smooth [33]. Equation 37 has a characteristic width of $1/\omega_{\rm C} = 1/(2\pi\nu_{\rm C})$, *implying that the pulse-width is controlled by coherence, in the absence of a form factor.* Figure 5 shows $\nu_{\rm C}$ versus the observer distance R and the shower width a.

Under the Lorentz gauge condition for Maxwell's equations, in the absence of static potentials, the negative derivative of the vector potential yields the electric field: $-\partial\mathbf{A}/\partial t = \mathbf{E}$. Using Eq. 37, the vector potential is

$$\frac{R\mathbf{A}(t_{\rm r},\theta_{\rm C})}{[\mathrm{V}\cdot\mathrm{s}]} \approx -2\hat{E}_0\omega_{\rm C} \begin{cases} \exp(2\omega_{\rm C}t_{\rm r}) & t_{\rm r} \le 0 \\ \exp(-2\omega_{\rm C}t_{\rm r}) & t_{\rm r} > 0 \end{cases} \tag{38}$$

Equation 16 of [31] is the vector potential at $\theta = \theta_{\rm C}$:

$$\frac{R\mathbf{A}(t_{\rm r},\theta_{\rm C})}{[\mathrm{V}\cdot\mathrm{s}]} = -E_0'\sin(\theta_{\rm C})\hat{e_\theta}\left(\exp(-2|t_{\rm r}|/x_0) + (1 + x_1|t_{\rm r}|)^{-x_2}\right) \tag{39}$$

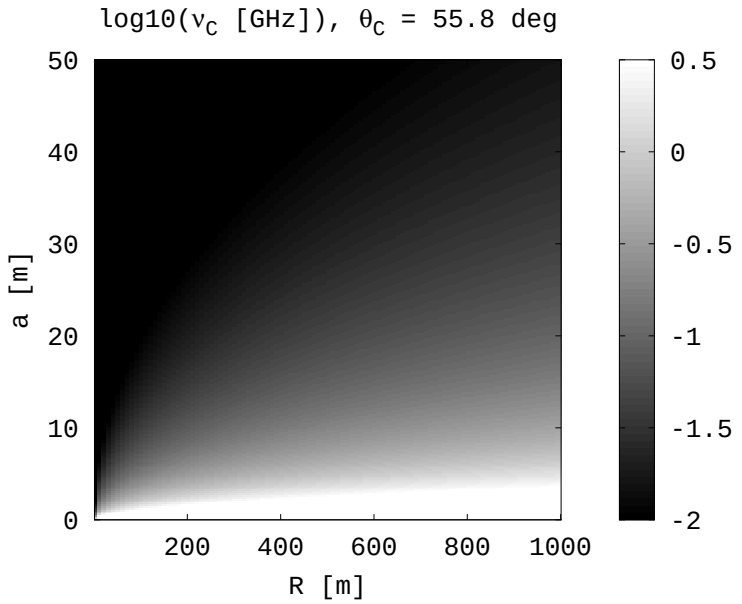

Figure 5: A contour plot of $\log_{10} \nu_{\rm C}$, for a parameter space relevant for ground-based radio-Askaryan detectors.

Eq. 39 is a formula that is used in MC by ARA/ARIANNA [28] [33] [49], corresponding to a fit to MC similar to ZHS. By comparing Eqs. 38 and 39, a natural, theoretical explanation of the fit parameters in [31] arises, albeit from a special case: $\widetilde{F} = 1$, and $x_0 = 1/(\omega_{\rm C})$, with $x_2 \gg 1$, or $x_1 \sim 0$. Thus, the result from [31] has been derived from first principles, rather than fitting to MC.

The fits in Ref. [31] have $x_2 \approx x_1 \approx 3$. The fact that x_1 and x_2 are not relevant to Eq. 38 is precisely because stipulating that $\widetilde{F}(\omega, \theta_{\rm C}) = 1$ leaves the spectral limiting to $\nu_{\rm C}$ rather than $\widetilde{F}(\omega, \theta)$. Such a scenario can be important when dealing with observations of cascades with $R = \mathcal{O}(100)$ m, under the influence of the LPM effect. In this case, only a small fraction of the shower excess profile is within $\Delta z_{\rm coh}$, and $\nu_{\rm C}$ cuts off the spectrum. Another example in which spectral limiting is due to $\nu_{\rm C}$, rather than $\widetilde{F}(\omega, \theta)$, is when the dielectric medium is denser than ice. The Askaryan spectra extends to $\approx \mathcal{O}(10)$ GHz at $\theta = \theta_{\rm C}$ in salt, for example [50]. Higher density leads to a more compact ICD, suppressing the effect of $\widetilde{F}(\omega, \theta)$. Figure 5 shows a parameter space for $\nu_{\rm C}$ relevant to ARA/ARIANNA.

The result $x_0 = 1/(\omega_{\rm C})$ also has a useful physical analogy for the shower width, a. Let the signal propagation time be T, such that (to first order) $R = cT/n$. Equation 40 then relates the

pulse width x_0 from Eq. 39 to the shower width a:

$$x_0 = \left(\frac{a\sin\theta_{\rm C}}{c}\right)\left(\frac{a\sin\theta_{\rm C}}{R}\right) = T\left(\frac{a\sin\theta_{\rm C}}{\sqrt{n}R}\right)^2 \tag{40}$$

Equation 40 demonstrates that the pulse width is a fraction of the propagation time T, and proportional to $(a/R)^2$.

4.2. The limit $\eta < 1$, $\sigma < 1$, $\widetilde{F}(\omega,\theta_{\rm C}) \neq 1$

Askaryan radiation from cascades experiences further low-pass filtering from $\widetilde{F}(\omega,\theta) \neq 1$ (Sec. 3.4). The parameter σ can be used to define a limiting frequency: $\sigma = \omega/\omega_{\rm CF}$, similar to $\eta = \omega/\omega_{\rm C}$. The electric field of Eq. 34, combined with the form factor $\widetilde{F}(\omega,\theta_{\rm C})$ of Eq. 26, is

$$\frac{R\widetilde{\mathbf{E}}(\omega,\theta_{\rm C})}{[\rm V/Hz]} = -\widetilde{F}(\omega,\theta)\frac{i\omega E_0\sin\theta_{\rm C}e^{i\omega R/c}}{(1-i\omega/\omega_{\rm C})^{1/2}}\hat{e_\theta} = -\frac{i\omega E_0\sin\theta_{\rm C}e^{i\omega R/c}}{(1-i\omega/\omega_{\rm C})^{1/2}(1+(\omega/\omega_{\rm CF})^2)^{3/2}}\hat{e_\theta} \tag{41}$$

In the limit $\sigma < 1$, and $\eta < 1$, Eq. 41 may be approximated as shown in Eq. 42, using $t_{\rm r} = t - R/c$, and $\omega_0 = \sqrt{2/3}\ \omega_{\rm CF}$.

$$\frac{R\mathbf{E}(t_{\rm r},\theta_{\rm C})}{[\rm V]} \approx \frac{i\omega_0^2\omega_{\rm C}}{\pi}\hat{E}_0\frac{d}{dt_{\rm r}}\oint d\omega\frac{e^{-it_{\rm r}\omega}}{(\omega+2i\omega_{\rm C})(\omega+i\omega_0)(\omega-i\omega_0)} \tag{42}$$

There are two poles in the lower-half complex plane, and one in the upper-half plane. If $t_{\rm r} > 0$, the contour integral around the lower infinite semi-circle converges because the numerator approaches zero exponentially as $\mathrm{Im}\{\omega\} \to -\infty$. Conversely for $t_{\rm r} < 0$, the contour integral converges along the upper infinite semi-circle. The final field is given by Eq. 43, to first-order in ϵ, with $\epsilon = \omega_0/\omega_{\rm C}$.

$$\frac{R\mathbf{E}(t_{\rm r},\theta_{\rm C})}{[\rm V]} \approx \frac{\hat{E}_0\omega_{\rm CF}^2}{3}\begin{cases}(1-\frac{1}{2}\epsilon)\exp(\omega_0 t_{\rm r}) & t_{\rm r}\leq 0\\ -\exp(-\omega_0 t_{\rm r}) + 2\exp(-2\omega_{\rm C}t_{\rm r}) & t_{\rm r} > 0\end{cases} \tag{43}$$

Consulting Fig. 5 reveals regions of parameter space where $\omega_{\rm C} \leq 1$ GHz. Consulting Eq. 23 and Eq. 35 shows that $\epsilon < 1$ is typical for cascades with $a \leq \mathcal{O}(1-10)$ m. The relative strengths of $\omega_{\rm C}$ and $\omega_{\rm CF} = \sqrt{3/2}\omega_0$ are shown in Fig. 6, versus the longitudinal and lateral cascade widths.

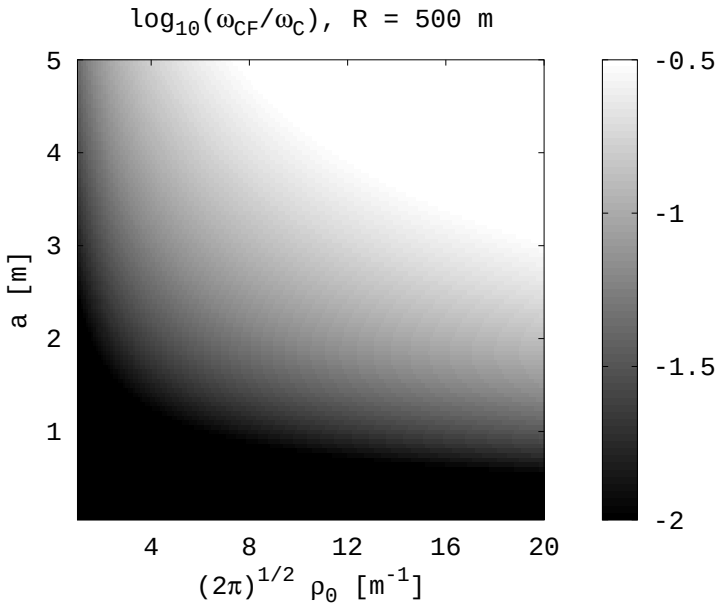

Figure 6: A contour plot of $\omega_{\rm CF}/\omega_{\rm C} = \nu_{\rm CF}/\nu_{\rm C}$, for a parameter space relevant for ground-based radio-Askaryan detectors.

The vector potential corresponding to Eq. 43 is

$$\frac{R\mathbf{A}(t_{\rm r},\theta_{\rm C})}{[{\rm V}\cdot{\rm s}]} \approx -\frac{\hat{E}_0\omega_{\rm CF}}{\sqrt{6}} \begin{cases} (1-\frac{1}{2}\epsilon)\exp(\omega_0 t_{\rm r}) & t_{\rm r}\le 0 \\ \exp(-\omega_0 t_{\rm r}) - \epsilon\exp(-2\omega_{\rm C} t_{\rm r}) & t_{\rm r} > 0 \end{cases} \tag{44}$$

Equations 43 and 44 show that the field remains bipolar but asymmetric, and asymmetric in time, from the interplay between coherence and the form factor. The pulse width is enhanced due to the presence of two different limiting frequencies, $\omega_0 = \sqrt{2/3}\omega_{\rm CF}$, and $\omega_{\rm C}$. Equation 45 defines a parameter showing the relative importance of the two limiting frequencies:

$$\epsilon' = \omega_{\rm CF}/\omega_{\rm C} = (\sqrt{2\pi}\rho_0\rho)\left(\frac{a}{R}\right)^2 \tag{45}$$

Fig. 6 is a contour graph of ϵ' in a parameter space relevant for ARA/ARIANNA. The first term in parentheses in Eq. 45 represents the relative importance of $\widetilde{F}(\omega,\theta)$. The second term in parentheses is the ratio of the longitudinal cascade width to the observer distance, represents the quality of the Fraunhofer limit.

4.3. Generalization of Eq. 41

The purpose of Eq. 32 is to account for excess charge at lateral distances greater than one Molière radius. Consequently, Eq. 41 may be generalized to

$$\frac{R\widetilde{\mathbf{E}}(\omega,\theta_{\rm C})}{[\rm V/Hz]} = -\sum_{j=0}^{N}\frac{\alpha_{\rm j} i\omega \hat{E}_0 e^{i\omega R/c}}{(1-i\omega/\omega_{\rm C})^{1/2}(1+(\omega/\omega_{\rm CF,j})^2)^{3/2}} \tag{46}$$

Making the same approximations leading up to Eq. 42, and exchanging the order of summation and integration, yields

$$\frac{R\mathbf{E}(t_{\rm r},\theta_{\rm C})}{[\rm V]} \approx \sum_{\rm j=0}^{N}\alpha_{\rm j}\frac{i\omega_{\rm C}\omega_{0,\rm j}^2}{\pi}\hat{E}_0\frac{d}{dt_{\rm r}}\oint d\omega\frac{e^{-it_{\rm r}\omega}}{(\omega+2i\omega_{\rm C})(\omega+i\omega_{0,\rm j})(\omega-i\omega_{0,\rm j})} \tag{47}$$

The summation terms of Eq. 47 are equal to Eq. 43, with the substitution $\omega_0 \rightarrow \omega_{0,\rm j}$:

$$\frac{R\mathbf{E}(t_{\rm r},\theta_{\rm C})}{[\rm V]} \approx \sum_{\rm j=0}^{N}\alpha_{\rm j}\frac{\hat{E}_0\omega_{0,\rm j}^2}{2}\begin{cases}(1-\frac{1}{2}\frac{\omega_{0,\rm j}}{\omega_{\rm C}})\exp(\omega_{0,\rm j}t_{\rm r}) & t_{\rm r}\le 0\\ -\exp(-\omega_{0,\rm j}t_{\rm r})+2\exp(-2\omega_{\rm C}t_{\rm r}) & t_{\rm r}>0\end{cases} \tag{48}$$

5. Summary

The Askaryan fields for a neutrino-induced high-energy cascade have been presented, accounting for the LPM effect, and $\widetilde{F}(\omega,\theta)$. The fully analytic calculations and associated code require no *a priori* MC analysis, making them computationally efficient and accurate. The cascade model has been verified independently, up to an energy of 0.1 EeV, and the lateral shower structure has been shown to be constant versus depth within the dielectric medium, near depths where the radiation is maximal. The code computes the entire field, for any frequencies, times, or viewing angles chosen by the user. Table 1 contains brief summary of the results and tools presented in this work.

The LPM effect is found to modify low-frequency emission, to suppress high-frequency emission, and to narrow the Cherenkov cone. The $\widetilde{F}(\omega,\theta)$ function smooths the field in contours of field strength versus time and viewing angle. $\widetilde{F}(\omega)$ is similar to a two-pole, low-pass filter, with the limiting frequency determined by cascade Molière radius. The θ-dependence in the form of $\widetilde{F}(\omega,\theta)$ implies that the filtered radiation depends on the laterally-projected wavevector. Finally, the field shows interesting causal structure that could serve as a discrimination technique between the distance R and the cascade energy, for *in situ* detectors such as ARA and ARIANNA.

Effect	Eq./Fig.	Sec.
Complete model $\hat{e}_\theta \cdot \widetilde{\mathbf{E}}(\omega, \theta)$	Fig. 3	Sec. 3.5
Complete model $\hat{e}_r \cdot \widetilde{\mathbf{E}}(\omega, \theta)$	Fig. 4	Sec. 3.5
Cascade Form Factor, $\widetilde{F}(\omega, \theta)$	Eq. 26	Sec. 3.4.2
$\mathbf{E}(t, \theta_{\mathrm{C}})$, $\widetilde{F}(\omega, \theta) = 1$, $\eta < 1$,	Eq. 37	Sec. 4.1
$\mathbf{E}(t, \theta_{\mathrm{C}})$, $\widetilde{F}(\omega, \theta) \neq 1$, $\eta < 1$,	Eq. 43	Sec. 4.2
$\omega_{\mathrm{CF}}/\omega_{\mathrm{C}}$ Figure of Merit	Eq. 45	Sec. 4.2

Table 1: A summary of specific results. Figures 3 and 4 may be reproduced using the open-source code: https://github.com/918particle/AskaryanModule.

Time-domain expressions were derived for the fields by computing the inverse Fourier transform of the RB model, under specific frequency limits. Future work will focus exclusively on the time domain, for viewing angles $\theta \neq \theta_{\mathrm{C}}$, and frequencies $\omega \approx \omega_{\mathrm{C}}$ and $\omega \approx \omega_{\mathrm{CF}}$. Having theoretical time-domain signals on hand facilitates Askaryan-based neutrino searches by allowing thermal fluctuations to be rejected on the basis of non-correlation with theoretical templates. Currently, *in situ* Askaryan-based detectors are limited by thermal noise. Rejecting the thermal noise in favour of neutrino signals is an exercise in the mathematical analysis of thermal fluctuations [51]. Armed with a firm theoretical understanding of the Askaryan effect, this challenge is made easier.

6. Acknowledgements

We thank the NSF for the support received under the NSF CAREER award 1255557, and for support from the NSF award for the Askaryan Radio Array (Grant 1404266). We are grateful to the Ohio Supercomputing Center [52] for their staff support, training, and resources. Contributions were also received from The Ohio State University, the Center for Cosmology and Astroparticle Physics (CCAPP), and the United States-Israel Binational Science Foundation Grant 2012077. We thank John Ralston and Roman Buniy for their helpful remarks regarding the mathematical physics. Also, special thanks are in order for John Beacom and Steve Barwick for practical advice.

7. Appendix

7.1. Causal Features and Poles of Askaryan Radiation

The complex pole-structure of the various models each demonstrate how the models treat the issue of causality. The E-field of ZHS, on-cone in Eq. 52 takes the form

$$\frac{R\widetilde{\mathbf{E}}}{[\mathrm{V/Hz}]} = -E_0\omega_0^2 \frac{i\omega}{(\omega + i\omega_0)(\omega - i\omega_0)}\hat{e}_\theta \tag{49}$$

Figure 16 of ZHS shows that the E-field phase is $\sim 90^\circ$ below 1 GHz, or a phase factor of $\exp(i\pi/2) = i$. The overall minus sign in Eq. 49 is just a convention. Taking the inverse Fourier transform, the time-domain form of the field at the Cherenkov angle may be written

$$\frac{R\mathbf{E}(t)}{[\mathrm{V}]} = \omega_0^2 E_0 \frac{d}{dt}\int_{-\infty}^{\infty} \frac{e^{-i\omega t}}{(\omega + i\omega_0)(\omega - i\omega_0)} d\omega \tag{50}$$

The integral converges via Jordan's lemma if the contour is the infinite upper semi-circle for $t < 0$, and, for $t > 0$, the infinite lower semi-circle. There is an overall minus sign from the clockwise contour. The result is

$$\frac{R\mathbf{E}(t)}{[\mathrm{V}]} = \omega_0^2 E_0 \hat{e_\theta} \begin{cases} \exp(\omega_0 t) & t \leq 0 \\ -\exp(-\omega_0 t) & t > 0 \end{cases} \tag{51}$$

The existence poles above and below the real line is deemed a causality violation by RB. Physically, the field changes overall sign when the angular acceleration of the charge relative to the observer changes sign. Feynman's formula [30] states that the field from an accelerating charge goes like $\mathbf{E} \propto \mathrm{sgn}(1 - n\hat{u}\cdot\vec{\beta})\hat{u}\times\ddot{\theta}$, where $\vec{\beta}$ is the velocity of the charge, and $\hat{u}$ is a unit vector at the charge location in the direction of the observer. $\mathbf{E}$ changes sign as the charge crosses the plane in which R is minimized. The quantity $\ddot{\theta}$ increases rapidly, until the plane crossing, after which it decreases rapidly.

From Eq. 50 $\widetilde{F}_{\mathrm{ZHS}}(\omega) \propto (\omega + i\omega_0)^{-1}(\omega - i\omega_0)^{-1}$. Treating $t > 0$ and $t < 0$ separately, the inverse Fourier transform of $\widetilde{F}_{\mathrm{ZHS}}(\omega)$ with respect to the coordinate ρ' yields $f(\mathbf{x}') \propto \exp(-\rho')$. Therefore, a logical inference is that *the full, 3D ICD responsible for* $\widetilde{F}(\omega,\theta)$ *is distributed exponentially.* Geant4 simulations show this to be correct in Sec. 7.3.

7.2. Spectral, Phase, and Angular Dependence

For cases in which $E_{\rm C} < E_{\rm LPM}$, the associated code agrees with the ZHS parameterization. Equations 10-13, via the associated code, are compared in Figs. 7-8 to Eqs. 52-53, which are Eqs. 20-21 from ZHS, with $\Delta\theta = 2.4^{\circ}(\nu_0/\nu)$, and $\nu_0 = 0.5$ GHz.

$$\frac{R|\widetilde{\mathbf{E}}(\omega, \theta = \theta_{\rm C})|}{\left[\frac{\rm V}{\rm MHz}\right]} = 1.1 \times 10^{-7} \frac{E_0}{[\rm TeV]} \left(\frac{\nu}{\nu_0}\right) \frac{1}{1 + (\nu/\nu_0)^2} \hat{e}_\theta \tag{52}$$

$$\widetilde{\mathbf{E}}(\omega, \theta) = \widetilde{\mathbf{E}}(\omega, \theta = \theta_{\rm C}) \exp\left[-\frac{1}{2}\left(\frac{\theta - \theta_{\rm C}}{\Delta\theta}\right)^2\right] \hat{e}_\theta \tag{53}$$

In Fig. 7 (left), the spectra are scaled by $R[\rm m]/E_{\rm C}[\rm TeV]$, where $E_{\rm C}$ is the cascade energy in TeV. In Fig. 7 (right), the angular dependence of RB and ZHS is compared. The factor $\widetilde{F}$ in Fig. 7 corresponds to a shower with a lateral ICD of exponential form, with a width of ~ 5 cm. The cone-width is also inversely proportional to a in the RB model - an important detail that accounts for cone-width narrowing under the influence of the LPM effect.

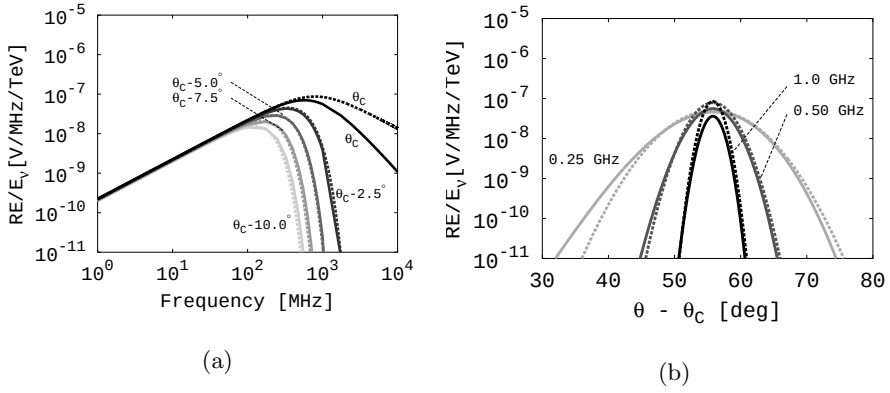

(a) (b)

Figure 7: (a) The spectrum from ZHS (dashed lines) and $|\hat{e}_\theta \cdot \widetilde{\mathbf{E}}(\omega)|$ from the code (solid lines), scaled by $R/E_{\rm C}$. The cascade width is $a = 1.5$ m, and $R = 1000$ m and $\widetilde{F} \neq 1$. (b) The angular dependence of the ZHS fits (dashed lines), compared to this work (solid lines).

The phase produced by the associated code is shown in Fig. 8, and compared to the ZHS result at the Cherenkov angle. The phases agree, up to frequencies at which the cone-width has attenuated the radiated power. Above these frequencies, the group delay (the slope of the phase) grows exponentially.

The spectral and angular dependence under the influence of the LPM effect and $\widetilde{F}(\omega)$ is shown in Fig. 9, revealing three effects. First, a low-frequency enhancement is caused by the cascade elongation, relative to ZHS. The effect is physical, as long as $\eta \lesssim 1$, so that the stretched a is still $\lesssim \Delta z_{\rm coh}$. Second, a high-frequency attenuation in the spectrum is expected if $ka \gg 1$: $\mathcal{W}(\eta, \theta) \propto \exp(-(ka)^2)$ in Eq. 13. Third, cone-width narrowing seen in Fig. 9 (right) follows from RB, where the cone-width is inversely proportional to a, and a has been stretched via the LPM effect.

7.3. Numerical Study of the Excess Charge Distribution

Geant4 [53] [54] is used to derive numbers for $\sqrt{2\pi}\rho_0$, and those results are checked with Eqs. 17-19. Refs. [46, 47, 48] are other works that used GEANT/Pythia to calculate Askaryan radiation properties. The GEANT4 high-energy electromagnetic option-1 physics list was used, with a MC threshold of 1 MeV, $e^{\pm}$ primaries, and ice of density 0.917 g/cm^3 and at a temperature of 240 K. Although the LPM effect is important primarily for electromagnetic cascades, $\widetilde{F}(\omega, \theta)$ does not depend on a, so it is also valid for hadronic cascades.

CPU memory constraints forbid accounting for all tracks, so a pre-shower/sub-shower approach is taken to access more memory. A pre-shower drops all particles with energy below 0.1 PeV. The trajectory, position and type of the pre-shower particles generated by the primary are recorded and sent to separate CPUs. Each particle in the pre-shower then becomes an independent cascade, with a second MC threshold of 1 MeV.

The lateral ICD is shown in Fig. 10 (a). The results follow $\propto \exp(-\sqrt{2\pi}\rho_0\rho')$ in the range

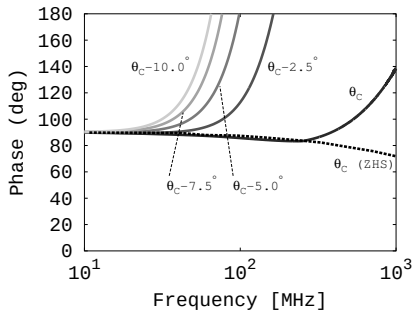

Figure 8: Phase of the Askaryan signal versus frequency. The dashed line is the ZHS result, at the Cherenkov angle. The code produces the solid lines at the given viewing angles.

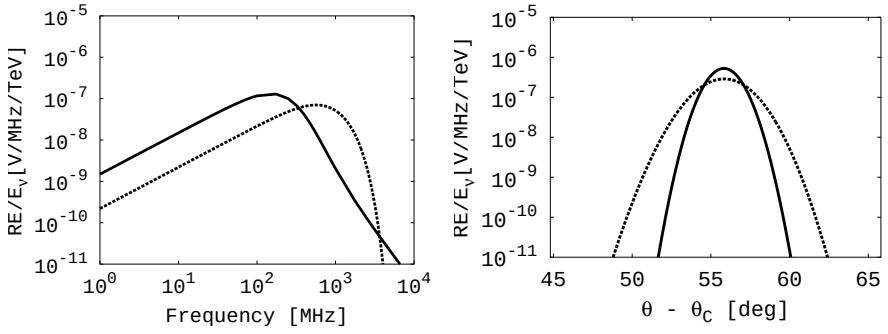

(a) (b)

Figure 9: (Left): $|\hat{e}_\theta \cdot \widetilde{\mathbf{E}}(\omega)|$, for $E_{\rm C} = 10$ PeV, $R = 1000$ m, and $\theta = 57^\circ$. The dashed line is the ZHS fit to Monte Carlo, and the solid line is the result from the associated code, with the LPM effect applied. (Right): The angular dependence of the same $|\hat{e}_\theta \cdot \widetilde{\mathbf{E}}(\omega)|$ as the solid line at (left), with the LPM effect applied (gray), and without it (black), at $\nu = 300$ MHz.

$\rho' = [0, \rho_1/d_{\rm ice}]$ (0-113 mm in ice, with $\rho_1 = 10.4$ g cm^{-2} and $d_{\rm ice} = 0.917$ g cm^{-3}). The gray data corresponds to Geant4 tracks inside a 100 PeV cascade, 25 ± 0.01 ns from the beginning of the first Geant4 interaction. The fit diverges only at radii where the radiation is ~ 1 % of the total signal.

The results for $\sqrt{2\pi}\rho_0$ are shown in Fig. 10 (b), averaged over 10 cascades with $E_{\rm C} = 100$ PeV. Each point contains tracks existing within 10 ps of the time on the x-axis. Early in the cascade, the particles have not yet diffused laterally, implying a higher value of $\sqrt{2\pi}\rho_0$. The dashed horizontal line represents the average between 15-35 ns, when lateral diffusion saturates.

The ICD per unit area, vs. Molière radius, is shown in Fig. 11 (a), plotted along with Eq. 19. Figure 11 (b) shows the fitted shower age s as a function of time after the first interaction. Eq. 19 was fit to the MC data sets at each time bin, with s as a free parameter. The results match the definition of s, from which the gray dashed line in Fig. 11 is derived.

Figure 12a matches Eq. 17 to MC data, neglecting photons, with a 1 MeV MC threshold. The Gaussian form is evident [55], justifying the RB saddle-point expansion. The ICD as a function of z' is shown in Fig. 12b. The width of $f(\mathbf{x}')$ versus z' is proportional to the width of the time-window (10 ps), justifying its approximation as a δ-function in $f(\mathbf{x}')$.

The parameter $n_{\rm max}$ in RB is the number of excess *negative* charges. The fractional excess charge is $\Delta q = (N_{\rm e^-} - N_{\rm e^+})/(N_{\rm e^-} + N_{\rm e^+})$, so $n_{\rm max} = N\Delta q$. The MC shows that Δq to is linear with depth. The y-intercept is sensitive to the MC threshold, but the slope is not. The associated

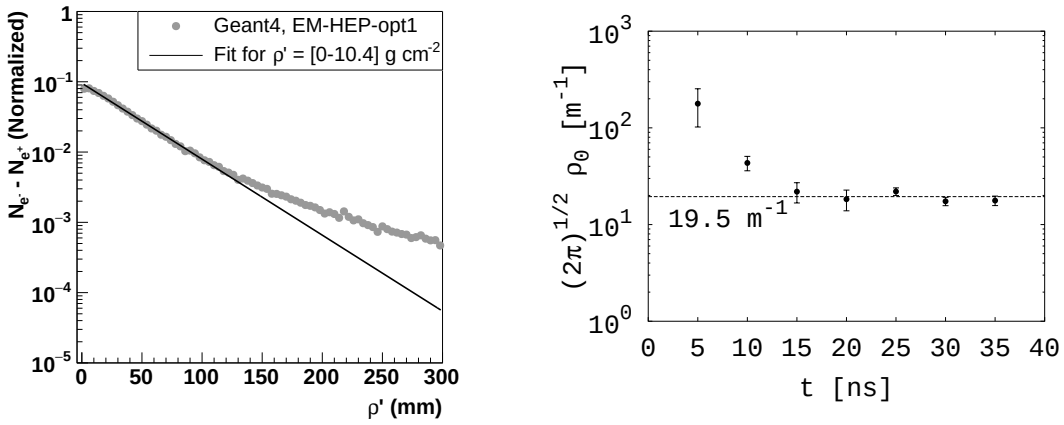

(a) (b)

Figure 10: (a) $N_{e^-} - N_{e^+}$, versus ρ' at 25 ns into a 100 PeV shower (gray points). The slope of the exponential is $\sqrt{2\pi}\rho_0$, by Eq. 21. The fit is between $\rho' = 0$ and $\rho' = 10.4$ g cm^{-2} in ice (one Molière radius), or 113 mm. (b) Fit results for the parameter $\sqrt{2\pi}\rho_0$ vs. time within the shower. The dashed line is the average of the points between 15-35 ns.

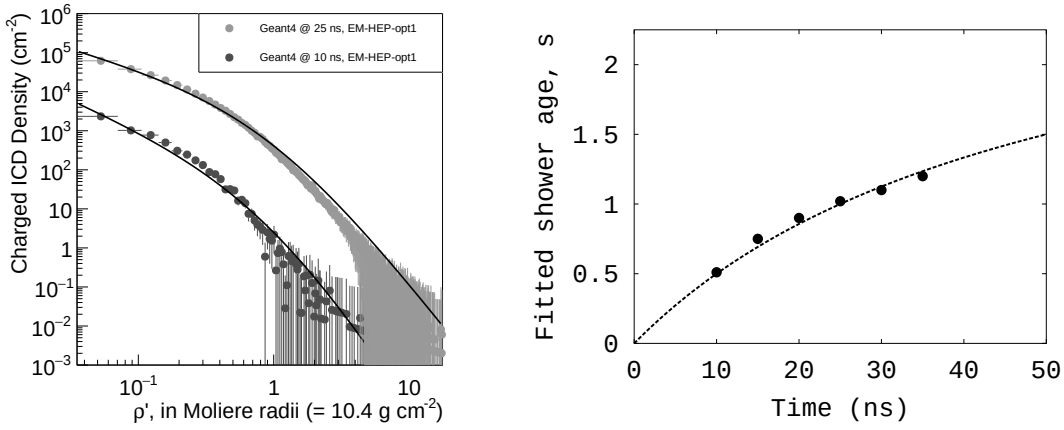

(a) (b)

Figure 11: (a) The charged ICD density, at 10 ns and 25 ns after the first interaction. The solid lines are fits of Equation 19 to the points with the shower age, s, as free parameter. (b) The fitted shower age, s, versus time since first interaction. The dashed line is the theoretical expectation.

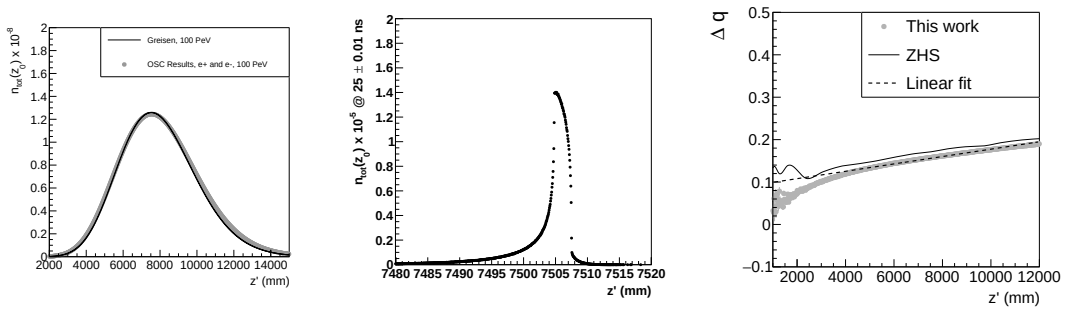

(a) (b) (c)

Figure 12: (a) $n_{\rm tot}$ versus z', for a 100 PeV cascade. (b) The ICD at 25 ± 0.01 ns after the first interaction. (c) The fractional negative charge excess of a 100 PeV shower, with a 5 MeV MC threshold from Geant4. The solid line is the ZHS result with a 5 MeV MC threshold, and the dashed line is a linear fit to the OSC results.

code includes the linear dependence of Δq on depth by sampling the linear fit at $z_{\rm max}$. Figure 12c shows Δq and that of ZHS.

References

[1] M. G. Aartsen, et al., First observation of pev-energy neutrinos with icecube, Phys. Rev. Lett. 111 (2013) 021103. doi:10.1103/PhysRevLett.111.021103.
URL http://link.aps.org/doi/10.1103/PhysRevLett.111.021103

[2] O. E. Kalashev, V. A. Kuzmin, D. V. Semikoz, G. Sigl, Ultrahigh-energy neutrino fluxes and their constraints, Phys. Rev. D 66 (2002) 063004. doi:10.1103/PhysRevD.66.063004.
URL http://link.aps.org/doi/10.1103/PhysRevD.66.063004

[3] K. Kotera, D. Allard, A. Olinto, Cosmogenic neutrinos: parameter space and detectabilty from pev to zev, Journal of Cosmology and Astroparticle Physics 2010 (10) (2010) 013.
URL http://stacks.iop.org/1475-7516/2010/i=10/a=013

[4] J. G. Learned, K. Manheim, High-energy neutrino astrophysics, Nuclear and Particle Science 50 (2000) 679–749. doi:10.1146/annurev.nucl.50.1.679.

[5] K. Greisen, End to the cosmic-ray spectrum?, Phys. Rev. Lett. 16 (1966) 748–750. doi:10.1103/PhysRevLett.16.748.
URL http://link.aps.org/doi/10.1103/PhysRevLett.16.748

[6] G. Zatsepin, V. Kuzmin, Pis ma zh. eksp. teor. fiz. 4,114 (1966)[jetp. lett. 4, 78 (1966)]. v. berezinsky and g. zatsepin, Phys. Lett. B 8 (1969) 423.

[7] E. Waxman, J. Bahcall, High energy neutrinos from astrophysical sources: An upper bound, Phys. Rev. D 59 (1998) 023002. doi:10.1103/PhysRevD.59.023002.

[8] R. Engel, D. Seckel, T. Stanev, Neutrinos from propagation of ultrahigh energy protons, Phys. Rev. D 64 (2001) 093010. doi:10.1103/PhysRevD.64.093010.

[9] K. Murase, M. Ahlers, B. C. Lacki, Testing the hadronuclear origin of pev neutrinos observed with icecube, Phys. Rev. D 88 (2013) 121301. doi:10.1103/PhysRevD.88.121301.
URL http://link.aps.org/doi/10.1103/PhysRevD.88.121301

[10] J. C. Joshi, W. Winter, N. Gupta, How many of the observed neutrino events can be described by cosmic ray interactions in the milky way?, Monthly Notices of the Royal Astronomical Society 439 (4) (2014) 3414–3419. doi:10.1093/mnras/stu189.

[11] A. Connolly, R. S. Thorne, D. Waters, Calculation of high energy neutrino-nucleon cross sections and uncertainties using the martin-stirling-thorne-watt parton distribution functions and implications for future experiments, Phys. Rev. D 83 (2011) 113009. doi:10.1103/PhysRevD.83.113009.
URL http://link.aps.org/doi/10.1103/PhysRevD.83.113009

[12] P. W. Gorham, A. Connolly, et al., Implications of ultrahigh energy neutrino flux constraints for lorentz-invariance violating cosmogenic neutrinos, Phys. Rev. D 86 (2012) 103006. doi:10.1103/PhysRevD.86.103006.
URL http://link.aps.org/doi/10.1103/PhysRevD.86.103006

[13] M. Ahlers, L. Anchordoqui, M. GonzalezGarcia, F. Halzen, S. Sarkar, {GZK} neutrinos after the fermi-lat diffuse photon flux measurement, Astroparticle Physics 34 (2) (2010) 106 – 115. doi:http://dx.doi.org/10.1016/j.astropartphys.2010.06.003.
URL http://www.sciencedirect.com/science/article/pii/S0927650510001155

[14] K. Murase, D. Guetta, M. Ahlers, Hidden cosmic-ray accelerators as an origin of tev-pev cosmic neutrinos, Phys. Rev. Lett. 116 (2016) 071101. doi:10.1103/PhysRevLett.116.071101.
URL http://link.aps.org/doi/10.1103/PhysRevLett.116.071101

[15] G. Askaryan, Excess negative charge of electron-photon shower and the coherent radiation originating from it. radiorecording of showers under the ground and on the moon, J. Phys. Soc. Japan 17 (Suppl A).

[16] D. Saltzberg, et al., Observation of the askaryan effect: Coherent microwave cherenkov emission from charge asymmetry in high-energy particle cascades, Phys. Rev. Lett. 86 (2001) 2802–2805. doi:10.1103/PhysRevLett.86.2802.
URL http://link.aps.org/doi/10.1103/PhysRevLett.86.2802

[17] P. W. Gorham, et al., Observations of the askaryan effect in ice, Phys. Rev. Lett. 99 (2007) 171101. doi:10.1103/PhysRevLett.99.171101.
URL http://link.aps.org/doi/10.1103/PhysRevLett.99.171101

[18] J. Hanson, Ross Ice Shelf Thickness, Radio-frequency Attenuation and Reflectivity: Implications for the ARIANNA UHE Neutrino Detector, International Cosmic Ray Conference 4 (2011) 169. doi:10.7529/ICRC2011/V04/0340.

[19] J. Hanson, et al., Radar absorption, basal reflection, thickness and polarization measurements from the ross ice shelf, antarctica, Jour. Glac. 61 (227) (2015) 438–446.

[20] D. Besson, et al., In situ radioglaciological measurements near taylor dome, antarctica and implications for ultra-high energy (uhe) neutrino astronomy, Astroparticle Physics 29 (2) (2008) 130 – 157. doi:http://dx.doi.org/10.1016/j.astropartphys.2007.12.004.
URL http://www.sciencedirect.com/science/article/pii/S0927650507001831

[21] I. Kravchenko, S. Hussain, D. Seckel, D. Besson, E. Fensholt, J. Ralston, J. Taylor, K. Ratzlaff, R. Young, Updated results from the rice experiment and future prospects for ultra-high energy neutrino detection at the south pole, Phys. Rev. D 85 (2012) 062004. doi:10.1103/PhysRevD.85.062004.
URL http://link.aps.org/doi/10.1103/PhysRevD.85.062004

[22] P. W. Gorham, et al., Observational constraints on the ultrahigh energy cosmic neutrino flux from the second flight of the anita experiment, Phys. Rev. D 82 (2010) 022004. doi:10.1103/PhysRevD.82.022004.

[23] P. Gorham, et al., The antarctic impulsive transient antenna ultra-high energy neutrino detector: Design, performance, and sensitivity for the 20062007 balloon flight, Astroparticle Physics 32 (1) (2009) 10 – 41. doi:http://dx.doi.org/10.1016/j.astropartphys.2009.05.003.
URL http://www.sciencedirect.com/science/article/pii/S0927650509000838

[24] S. Barwick, et al., A first search for cosmogenic neutrinos with the {ARIANNA} hexagonal radio array, Astroparticle Physics 70 (2015) 12 – 26. doi:http://dx.doi.org/10.1016/j.astropartphys.2015.04.002.

[25] S. Barwick, et al., Time-domain response of the {ARIANNA} detector, Astroparticle Physics 62 (2015) 139 – 151. doi:http://dx.doi.org/10.1016/j.astropartphys.2014.09.002.

[26] S. W. Barwick, E. C. Berg, D. Z. Besson, T. Duffin, J. C. Hanson, S. R. Klein, S. A. Kleinfelder, K. Ratzlaff, C. Reed, M. Roumi, T. Stezelberger, J. Tatar, J. Walker, R. Young, L. Zou, Design and performance of the arianna hra-3 neutrino detector systems, IEEE Transactions on Nuclear Science 62 (5) (2015) 2202–2215. doi:10.1109/TNS.2015.2468182.

[27] P. Allison, et al., First constraints on the ultra-high energy neutrino flux from a prototype station of the askaryan radio array, Astroparticle Physics 70 (2015) 62 – 80. doi:http://dx.doi.org/10.1016/j.astropartphys.2015.04.006.

[28] P. Allison, et al., Design and initial performance of the askaryan radio array prototype eev neutrino detector at the south pole, Astroparticle Physics 35 (7) (2012) 457 – 477. doi:http://dx.doi.org/10.1016/j.astropartphys.2011.11.010.
URL http://www.sciencedirect.com/science/article/pii/S092765051100209X

[29] P. Gorham, F. Baginski, P. Allison, K. Liewer, C. Miki, B. Hill, G. Varner, The exavolt antenna: A large-aperture, balloon-embedded antenna for ultra-high energy particle detection, Astroparticle Physics 35 (5) (2011) 242 – 256. doi:http://dx.doi.org/10.1016/j.astropartphys.2011.08.004.
URL http://www.sciencedirect.com/science/article/pii/S0927650511001629

[30] E. Zas, F. Halzen, T. Stanev, Electromagnetic pulses from high-energy showers: Implications for neutrino detection, Phys. Rev. D 45 (1992) 362–376. doi:10.1103/PhysRevD.45.362.

[31] J. Alvarez-Muñiz, A. Romero-Wolf, E. Zas, Practical and accurate calculations of askaryan radiation, Phys. Rev. D 84 (2011) 103003. doi:10.1103/PhysRevD.84.103003.

[32] J. Alvarez-Muñiz, A. Romero-Wolf, E. Zas, Čerenkov radio pulses from electromagnetic showers in the time domain, Phys. Rev. D 81 (2010) 123009. doi:10.1103/PhysRevD.81.123009.

[33] E. Hong, Searching for ultra-high energy neutrinos with data from a prototype station of the askaryan radio array, Ph.D. thesis, The Ohio State University (2014).

[34] R. V. Buniy, J. P. Ralston, Radio detection of high energy particles: Coherence versus multiple scales, Phys. Rev. D 65 (2001) 016003. doi:10.1103/PhysRevD.65.016003.

[35] K. GREISEN, Progress in cosmic ray physics. j. g. wilson, ed. amsterdam: North-holland pub.; new york: Interscience, 1952. 557 pp., Science 115 (2990) (1952) 426–427. doi:10.1126/science.115.2990.426-a.

[36] Bogorodsky, V.V., and Bentley, C.R., and Gudmandsen P.E., Radioglaciology, D. Reidel Publishing Co., 1985.

[37] S. Klein, Suppression of bremsstrahlung and pair production due to environmental factors, Rev. Mod. Phys. 71 (1999) 1501–1538. doi:10.1103/RevModPhys.71.1501.
URL http://link.aps.org/doi/10.1103/RevModPhys.71.1501

[38] J. Alvarez-Muiz, E. Zas, Cherenkov radio pulses from eev neutrino interactions: the lpm effect, Physics Letters B 411 (1) (1997) 218 – 224. doi:http://dx.doi.org/10.1016/S0370-2693(97)01009-5.
URL http://www.sciencedirect.com/science/article/pii/S0370269397010095

[39] L. Gerhardt, S. Klein, Electron and photon interactions in the regime of strong landau-pomeranchuk-migdal suppression, Physical Review D 82 (7). doi:10.1103/physrevd.82.074017.

[40] A. Cillis, H. Fanchiotti, G. C. Canal, S. Sciutto, Influence of the LPM effect and dielectric suppression on particle air showers, Phys Rev D 59 (11) (1999) 113012. doi:10.1103/PhysRevD.59.113012.

[41] J. Alvarez-Muiz, E. Zas, The {LPM} effect for eev hadronic showers in ice: implications for radio detection of neutrinos, Physics Letters B 434 (34) (1998) 396 – 406. doi:http://dx.doi.org/10.1016/S0370-2693(98)00905-8.
URL http://www.sciencedirect.com/science/article/pii/S0370269398009058

[42] C. Hu, C. Chen, P. Chen, Near-field effects of cherenkov radiation induced by ultra high energy cosmic neutrinos, Astropart Phys 35 (7) (2012) 421–434. doi:10.1016/j.astropartphys.2011.11.008.

[43] T. Gaisser, A. Hillas, Reliability of the method of constant intensity cuts for reconstructing the average development of vertical showers, Proceedings of the 15th International Cosmic Ray Conference 8.

[44] G. Daniel, A. Jaime, W. R. Carvalho, R. Andrés, E. Zas, Calculations of electric fields for radio detection of Ultra-High energy particles, Phys Rev D 87 (023003). doi:10.1103/physrevd.87.023003.

[45] P. Allison, et al., Near-field effects of cherenkov radiation induced by ultra high energy cosmic

neutrinos, Astroparticle Physics 35 (2012) 421 – 434. doi:10.1016/j.astropartphys.2011.11.008.

[46] S. R. et. al., Coherent radio pulses from geant generated electromagnetic showers in ice, Phys. Rev. D 65 (103002). doi:10.1103/PhysRevD.65.103002.

[47] J. A.-M. et. al., Comparative study of electromagnetic shower track lengths in water and implications for cernekov radio emission, Phys. Rev. D 68 (043001). doi:10.1103/PhysRevD.68.043001.

[48] D. W. McKay, S. Hussain, Comparative study of radio pulses from simulated hadron-, electron-, and neutrino-initiated showers in ice in the gev-pev range, Phys. Rev. D 70 (103003). doi:10.1103/PhysRevD.70.103003.

[49] J. Hanson, The performance and initial results of the arianna prototype, Ph.D. thesis, The University of California, Irvine (2013).

[50] P. Miočinović, et al., Time-domain measurement of broadband coherent cherenkov radiation, Phys. Rev. D 74 (2006) 043002. doi:10.1103/PhysRevD.74.043002.

[51] S. O. Rice, Mathematical analysis of random noise, The Bell System Technical Journal 23 (3) (1944) 282–332. doi:10.1002/j.1538-7305.1944.tb00874.x.

[52] O. S. Center, Ohio supercomputer center, http://osc.edu/ark:/19495/f5s1ph73 (1987).

[53] S. Agostinelli, et al., Geant4 a simulation toolkit, Nuclear Instruments and Methods in Physics Research Section A: Accelerators, Spectrometers, Detectors and Associated Equipment 506 (3) (2003) 250 – 303. doi:http://dx.doi.org/10.1016/S0168-9002(03)01368-8.

[54] J. Allison, et al., Geant4 developments and applications, IEEE Transactions on Nuclear Science 53 (1) (2006) 270–278.

[55] B. Rossi, High-energy particles, NJ, 1952.